Dynamics of intraseasonal oscillations in the Bay of Bengal during summer monsoons captured by mooring observations

A. Pirro [a,*], H.W. Wijesekera [b], E. Jarosz [b], H.J.S. Fernando [a,c]

[a] *University of Notre Dame, Department of Civil Engineering, Environmental and Earth Sciences, Notre Dame, IN, 46556, USA*
[b] *Naval Research Laboratory, Stennis Space Center, MS, 39529, USA*
[c] *University of Notre Dame, Department of Aerospace and Mechanical Engineering, Notre Dame, IN, 46556, USA*

A B S T R A C T

The intraseasonal variabilities of current and temperature in the southern Bay of Bengal (BoB) were examined using in-situ observations collected in the upper 500 m of the water column for a period of 20 months, between December 2013 and August 2015. Data were sampled by six subsurface moorings deployed by the United States Naval Research Laboratory as part of an international effort focused on the dynamics of the northern Indian Ocean. The moored observations captured motions of multiple time-scales, including seasonal circulations, eddies, and planetary waves that underlie intraseasonal variability. This study focuses on 30–60-day intra-seasonal oscillations (ISOs). Spectral analysis of currents shows enhanced energy and momentum fluxes for the period 46–52-days. The ISO velocity fluctuations were coherent in the upper 500 m of the water column, strongest near the surface and nearly uniform below 100 m. The ISO kinetic energy appeared at the beginning of the 2014 summer monsoon and lasted throughout the summer, but the associated potential energy dropped rapidly after it peaked at the beginning of the monsoon season.

The correlation between the 30–60 day ISOs of local winds and the oceanic variability below 120 m depth was fund to be as small as 25% suggesting thus that the local winds were not the main forcing mechanism for ISOs. The 30–60-day band-passed sea-surface-height anomalies indicate westward propagating anomalies with phase speeds between 0.17 m s^{-1} at 8°N and 0.43 m s^{-1} at 4°N, within the phase-speed ranges of mode-1 and mode-2 linear baroclinic Rossby waves, pointing to the role of Rossby waves in 30–60-day ISOs.

The background mean flow acceleration resulting from the meridional divergence of wave momentum flux in the thermocline was about 10^{-8} m s^{-2}. As a result, within a wave period, ISOs can enhance the eastward flow in the thermocline by about 25%. The negative shear production computed for the same period is consistent with this finding, suggesting that the mean flow has gained kinetic energy at the expense of the ISO band at a rate of about 0.5×10^{-8} m^2 s^{-2}. The meridional heat-flux divergence was -10^{-7} °C s^{-1}, and has a tendency for cooling the thermocline by about 0.5 °C when the ISOs are active. The ISOs appear to play an important role in the ocean dynamics of the southern BoB during the summer monsoon.

1. Introduction

The oceanic circulation in the Indian Ocean (IO) is unique, signified by seasonal flow reversals, significant freshwater input, basin exchanges, variability of local forcing and remote forcing via planetary waves. Although previous work (e.g. Lighthill, 1969; Cox, 1970; Luther and O' Brien, 1985) shows that the semiannual reversal of currents in the Bay of Bengal (BoB) is closely related to monsoon winds, the details are complicated in that numerical experiments demonstrate the influence of remote forcing from the interior of the equatorial IO, which is

also related to monsoon winds (Yu et al., 1991; Clarke and Liu, 1993). Equatorial Kelvin waves, commonly interpreted as Wyrtki (1973) jets, propagate eastward along the equator during April/May and September/October. Upon reflection from the IO eastern boundaries, energy of Wyrtki jets is reflected back in part as long Rossby waves that disperse slowly and reach the central-eastern BoB during July–August (Han et al., 1999, 2001; Han, 2005; Nagura and McPhaden, 2010). The remaining energy is partitioned into two coastally-trapped Kelvin waves traveling poleward (Moore, 1968), which excite long Rossby waves propagating westward. Therefore, it is believed that planetary waves driven by

---

remote forcing from the interior of the IO contribute significantly to the formation, strength and intensity of BoB circulation (Nagura and McPhaden, 2010; Chen et al., 2015). A subset of these planetary waves is the mainstay of intraseasonal oscillations (ISOs), a sub-seasonal phenomenon with periods less than 120 days. The genesis of oceanic ISOs has been attributed to two mechanisms: external forcing (e.g. atmospheric ISOs and Ekman pumping) and internal processes (e.g. barotropic and baroclinic instabilities). Observations in the IO have captured a range of variabilities in the 30–120 days frequency band (e.g. Girishkumar et al., 2013), and past research has identified roughly three distinct ISO bands in the context of the thermocline: 30–60 days, 60–90 days, and 120 days (Han et al., 2001; Girishkumar et al., 2013).

ISOs are an important part of upper-ocean dynamics, and they affect air-sea interactions, for example, by determining the local sea-surface temperature (SST) and horizontal heat transport through non-linear mechanisms (Waliser et al., 2003, 2004; Jochum and Murtugudde, 2005). Oceanic ISOs also influence the atmospheric boundary layer by modifying surface heat fluxes and deep convection in the tropical atmosphere (Thum et al., 2002; Raymond et al., 2004). Strong ISOs are ubiquitous in the equatorial IO, from the far east (off the Indonesian Seas) to the central equatorial IO near Gan Island, Maldives (to name a few, McPhaden, 1982, Moore and McCreary, 1990; Qiu et al., 1999; Reppin et al., 1999; Sengupta et al., 2004; Han, 2005; Iskandar et al., 2005, 2006; Goswami, 2005; Miyama et al., 2006; Fu, 2007; Girishkumar et al., 2011). In the far-eastern IO at Benoa (8°42′S, 115°12′E) and Christmas Island (10°24′S, 105°42′E), a strong 90-day peak in sea level has been recorded by tide-gauge measurements while near the Timor Passage (11°18′S, 122°54′E) both 80-90-day and 30-60-day oscillations have been found (Qiu et al., 1999). Simulations of Han et al. (2001) and Han (2005) suggest that different ISOs within 20-90 days are forced by different mechanisms, for example, 30-60 day oscillations by the Madden-Julian Oscillations and the second-baroclinic wave modes by the 90-day wind (Han, 2005). The baroclinic Rossby wave modes play an important role in the thermohaline structure of the BoB (Oliver and Thompson, 2010; Vialard et al., 2009; Webber et al., 2010, 2012; Girishkumar et al., 2013).

Planetary wave dynamics, both locally and remotely forced, and their interaction with the background flow (defined here as currents with variability > 120 days) clearly generate a repertoire of ISOs that contribute to the complexity of the IO circulation. Cheng et al. (2013) showed that non-linear Rossby waves propagating from the eastern BOB may account for most of the sea-surface-height-anomaly (SSHA) variance east of Sri Lanka, rather than the local wind-forced variability which accounted for only about 20% of the variability, and demonstrated non-linear energy transfer between different frequency bands. According to Sengupta et al. (2001), ISOs in the off-equatorial upper-ocean zonal currents south and east of Sri Lanka are due to a series of vortices generated when the westward propagating Rossby waves encounter the eastward-flowing Southwest Monsoon Current (SMC). Such vortex structures (eddies) can also be generated by the barotropic instability of the SMC (Pirro et al.,2020), have high 'total (kinetic plus potential) energy' content, and are capable of transferring energy to the mean flow (Cheng et al., 2013), with the latter leading to the intensification of the SMC Vinayachandran et al. (1999) via an up-gradient eddy-potential-vorticity flux (Rath et al., 2017). Eddies and ISOs may co-exist, and identification of their roles using observations are a challenge.

This paper describes 30–60 day ISOs in the thermocline of the BoB, based on long-term mooring observations, and investigates the formation and impacts of ISOs on the thermocline variability and background flow. This study was motivated by previous work that revealed a correlation between SST variability and 30–60-day summer ISOs in the BoB (Webster et al., 1998; Vecchi and Harrison, 2002; Rajendran and Kitoh, 2006; Roxy and Tanimoto, 2007), wherein improved predictability has been noted when such variability is accounted for. Interactions between the background flow and ISOs in the IO are fundamentally important,

yet no observations exist for relevant investigations. Lacking long time-series of water column observations, studies of ISOs have relied on modeling and satellite observations. To this end, as a part of the Office of Naval Research's ASIRI program (2012–2017) and a companion program by the Naval Research Laboratory (NRL) dubbed EBOB (Effects of Bay of Bengal Freshwater Flux on Indian Ocean Monsoon), key hydrophysical variables were sampled between December 2013 and August 2015 using an array of 6 deep mooring array deployed in the southern BoB. The energy, heat, and momentum fluxes, inter alia, were evaluated for the depth range of ~100–500 m to address our research goals. It is assumed that 30–60 day variability in this depth range is mainly contributed by the ISOs, and eddies generated by instabilities are mainly confined to the upper 100 m.

The paper is organized as follows. Instrumentation, moored data sets and background flow description are reported in Section 2. Descriptions of ISOs using mooring data and satellite SSH anomalies are provided in Section 3. The role of the local wind forcing on the 30–60-day ISOs is presented in Section 4. The impacts of ISOs on the thermocline based on meridional heat-flux and momentum-flux divergence are discussed in Section 5. Summary and conclusions are presented in Section 6. Derivations of energetics and Eliassen-Palm flux or "EP-flux" are provided in Appendix A.

2. Instrumentation, moored data sets, and background flow

2.1. Instrumentation and moored data sets

Six deep moorings were deployed in a triangular array in the southern BoB between December 2013 and August 2015 (Fig. 1). The moorings were located about 200 nm (370 km) east of Sri Lanka in the international waters at water depths between 3600 m and 3900 m (Fig. 1). The moorings contained acoustic Doppler current profilers (ADCPs) and a variety of instruments for recording temperature, conductivity, and pressure. Each mooring contained an upward-looking 300 kHz Teledyne RD Instruments Workhorse ADCP and a downward-looking 75 kHz Teledyne RD Instruments Long Ranger ADCP, both mounted in a Flotation Technology buoy, 45 inch (114 cm) in diameter, at depths between 16 m and 72 m. The moorings are fully described by Wijesekera et al. (2016b), and were designed to capture space-time scales of the currents and the physical properties in the upper 500 m.

Each mooring had twelve to fourteen temperature (T) sensors, three to four temperature and conductivity (TC) sensors, and four to six T, conductivity (C), and pressure (TCP) sensors mounted along the mooring cable beneath the ADCP buoy. These instruments consisted of
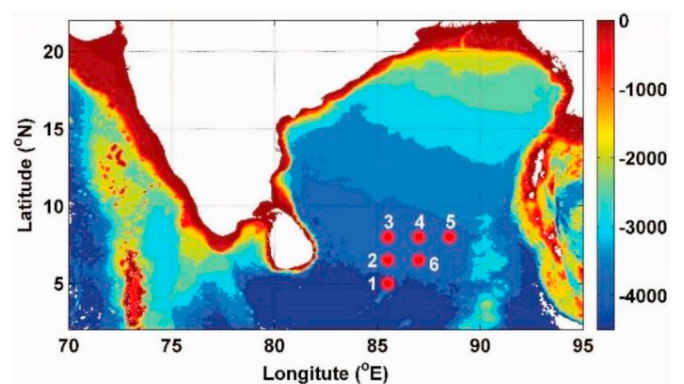

Fig. 1. Locations of NRL moorings in the southern Bay of Bengal are marked in red circles; NRL1: 85.5°E, 5.0°N, NRL2: 85.5°E, 6.5°N, NRL3: 85.5°E, 8.0°N, NRL4: 87.0°E, 8.0°N, NRL5: 88.5°E, 8.0°N, NRL6: 87.0°E, 6.5°N. The color image shows the bottom bathymetry in meters. (For interpretation of the references to color in this figure legend, the reader is referred to the Web version of this article.)

MicroCats (by Sea-Bird Electronics®), both with and without P sensors, to record the T and C; T data loggers (Vemco®); C, T, and depth (CTD) loggers (Aqua TROLL®); and CTD loggers (Star Oddi®, Aqua Troll®). Sampling rates were one minute for the Vemco recorders and ten minutes for others. These sensors were unevenly spaced and were densest around ~70 m from the buoy where strong stratification was expected; see Table 2 in Wijesekera et al. (2016b) for details.

Current profiles were measured from ~5 m to depths of ~500 m. Currents were sampled either every hour or half hour by the Long Ranger ADCP and Workhorse ADCP, respectively. Ping rate was 1 ping every 2 min (30 pings per hour) for the Long Ranger ADCP. In order to reduce surface-wave contamination in the Workhorse ADCP measurements, 40 pings were collected at 1 Hz at the beginning of each 30-minute sampling period. Vertical depth resolutions for the current measurements were 8 m and 2 m, for the Long Ranger and Workhorse, respectively. The accuracy of the Workhorse is 0.5% of the water velocity and the accuracy of the Long Ranger is 1% of the water velocity.

Mostly full data records were retrieved, except from the Long Ranger ADCP at NRL 4 which stopped after about 15 months. Thus, we present results only from five of the six moorings. The velocity data were gridded using the pressure data, and interpolated to common depth levels to compensate for mooring dips. The processing of the ADCP and raw data are described in detail in Wijesekera et al. (2016b). The vertical bin separation in the processed series is 8 m. Given significant data dropouts in the lower bins of the Workhorse records and upper bins of the Long Ranger records, some vertical interpolation was required. The data were then subsampled at 32 m, starting at 8 m and extending to 480 m, resulting in a time series of zonal (U) and meridional (V) velocity profiles at each of the mooring sites.

The depths of T and C sensors were evaluated by interpolating the pressure records of the ADCPs and TCP sensors in conjunction with their known locations on the mooring lines. The T was gridded at 4-m depth intervals within 50 m-400 m in depth, but the S was limited to four to six sensors within 50 m-200 m in depth and were not interpolated vertically. The processing of T and S data is described in detail by Wijesekera et al. (2016b), and 1-minute T data from the Vemco sensors are described in Wijesekera et al. (2019).

2.2. Mean currents and eddies

The (U, V) and T fields for each mooring were analyzed as follows. The time-depth series of U, V, and T were divided into background flow and fluctuating fields, where the first one represents low-frequency motions of timescales >120 days, larger or comparable to seasonal time scales, and ISOs represent fluctuations of time scales 30–90-days. Background velocity (U, V) and temperature (T), were obtained by applying a 120-day low-pass filter to the corresponding time-depth series. The cutoff period of 120 days was chosen since it is well above the residence period of mesoscale eddies in the region whereas periods >120 days represent seasonal variability (e.g. Rath et al., 2017). In subsequent analysis, ISOs were categorized into 30–60-day and 60-90-day bands.

Following Wijesekera et al. (2016b), below we briefly describe aspects of the seasonal flow and eddies relevant to ISOs. Figs. 2 and 4 display, respectively, the low-frequency currents (U, V) in the upper 500 m and T in the thermocline between 90 m and 388 m (except for NRL3 which recorded data only down to 310 m). Winds, from the daily Coupled ECMWF ReAnalysis (CERA-SAT) dataset provided by the European Centre for Medium-Range Weather Forecasts (ECMWF), with a spatial resolution of 1° and for the period of January 2014–August 2015,
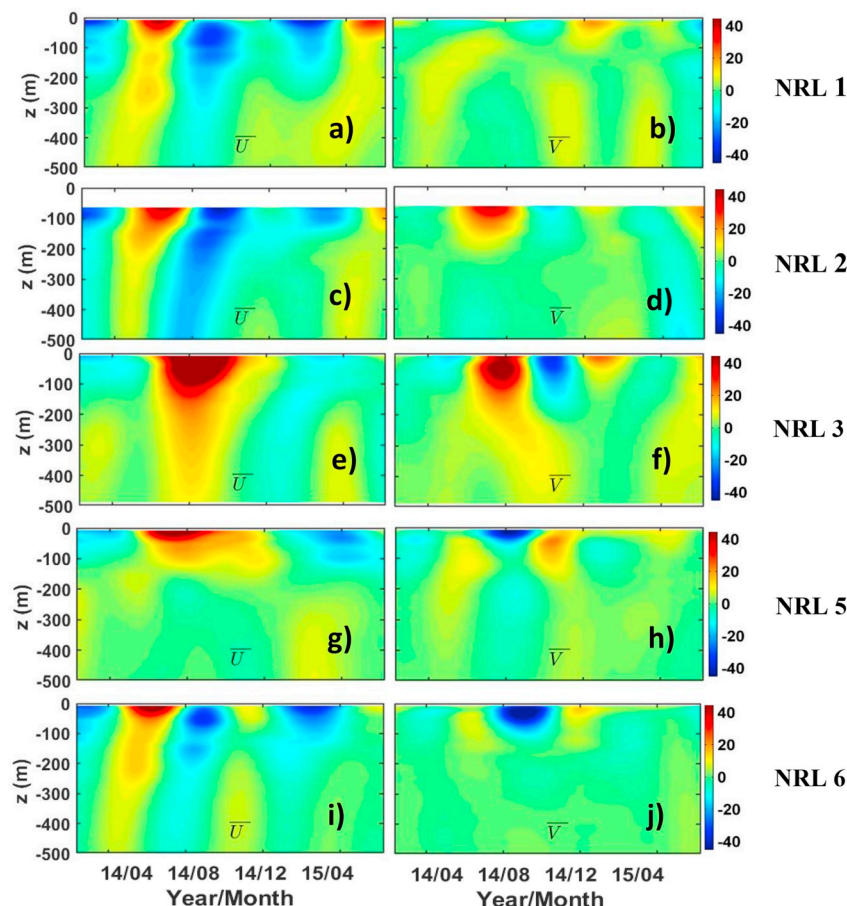

Fig. 2. Zonal and meridional seasonal currents (120-day filtered signals) at mooring locations. Units are in cm s^{-1}.

show that flow reversals follow the seasonal changes of surface winds (Fig. 5a).

The (U, V) and T fields (Figs. 2 and 4) reveal the passage of diverse dynamical features through the mooring array, for example, cyclonic and anticyclonic eddies, SMC and winter monsoon current (WMC). The mooring array captured a large cyclonic eddy, referred to as the Sri Lanka Dome (SLD), in July 2014 and an even larger Anticyclonic Eddy (AE) in August of 2014 (Fig. 10a and b in Wijesekera et al., 2016b and Lozovatsky et al., 2016), with spatial scales 200–300 km. The SMC flowed eastward between the SLD and the AE. The velocity at NRL2 (Fig. 2c and d) and NRL3 (Fig. 2e and f) show currents in excess of $40 \, \text{cm s}^{-1}$ in the upper 150 m in June–July 2014. Currents at NRL5 (Fig. 2g and h) and NRL6 (Fig. 2i and j) were weaker than those at NRL2 and NRL3, and were confined to the upper 80 m. U and V were about $10 \, \text{cm s}^{-1}$ below 200 m. Reversing currents (Fig. 2) indicate the passage of cyclonic and anticyclonic eddies in the upper layer and also wave-like signals especially below 200 m (see also Wijesekera et al., 2016c). Wijesekera et al. (2016b) suggest that the water exchange in the interior of the BoB may be largely influenced by the location and strength of the two eddies that modify the path of the SMC, but distinguishing the velocity fields associated with SMC and eddies is not straightforward.

During the passage of the SLD through the mooring array, isotherms rose up rapidly, thus forming a core of cold water with T typically less than 25 °C. At NRL3 (Fig. 3c), the isotherms rose about 50 m within a couple of weeks, indicating an upwelling speed of about 3.4 to $4.6 \times 10^{-3} \, \text{cm s}^{-1}$ (3–4 m d^{-1}) between 50 and 100 m. The seasonal cycle of the SSHA closely followed the thermocline (e.g. 20 °C isotherm) displacement (Wijesekera et al., 2016b). The 120-day low-pass-filtered SSHA fluctuations, the 20 °C isotherm-depth fluctuations, and the depth-averaged-current fluctuations in the upper 200 m propagated westward at a speed of about $10 \, \text{cm s}^{-1}$ (see Figs. 5 and 6 in Wijesekera et al., 2016c). Similarly, at NRL 1, 2 and 6 (Fig. 2a, c, i), a clear upward-phase propagation was evident. It is likely that these westward seasonal thermocline fluctuations are related to baroclinic Rossby waves as described in Subrahmanyam et al. (2001) and Girishkumar et al. (2011). These fluctuations were not visible at higher latitudes (e.g. NRL3 and 5) since eastward velocity of the SMC passing through 8°N dominated the signal.

Both the SLD and the AE eddy generate strong vertical velocities, about 4.6 to $5.8 \times 10^{-3} \, \text{cm s}^{-1}$ (4-5 m d^{-1}) at 25 m, and the estimated vertical relative vorticity was 20%-80% of the inertial frequency at 6.5°N (Wijesekera et al., 2016b). The estimated residence time of eddies observed in July–August 2014 was about 38-48 days (for ~200–300 km size and 5–6 cm s^{-1} speed), indicating that the time-domain filter used here to isolate 30–60-day oscillations may contain some eddy variability in the upper 100 m (Section 3).
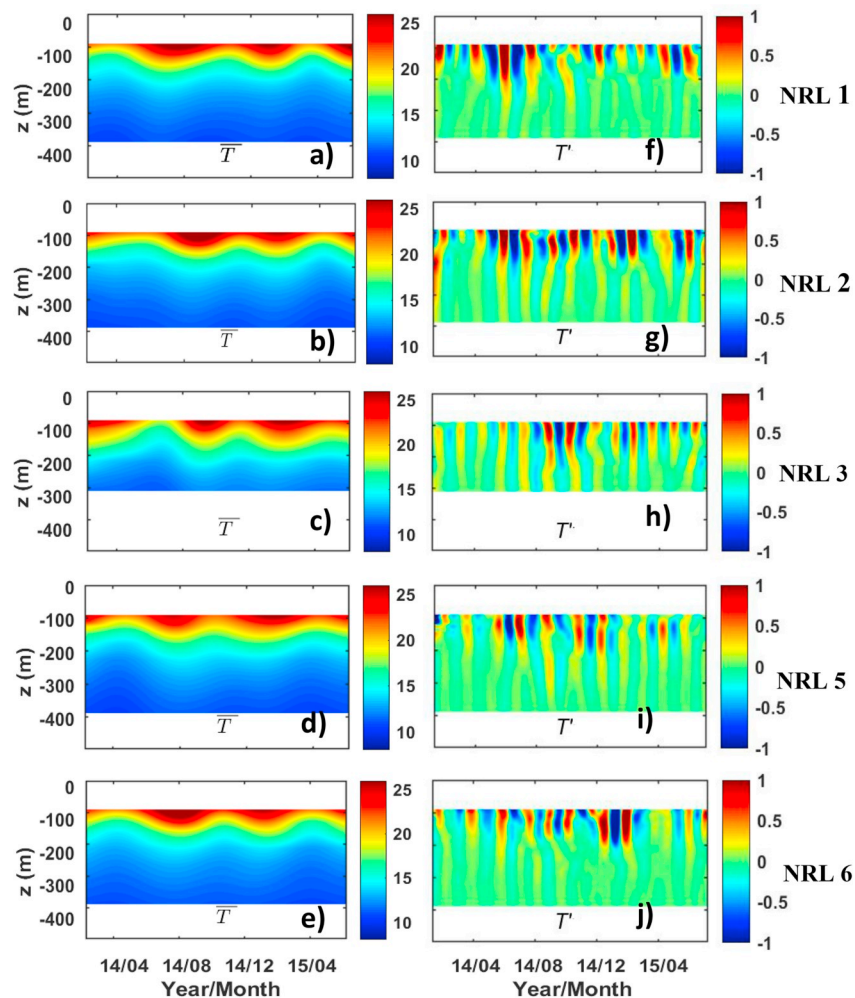

Fig. 3. Left panels: Seasonal temperature records (120 day filtered signals) at mooring locations. Right panels: Intraseasonal temperature records (30–60 day filtered signals) at mooring locations. Units are in °C.
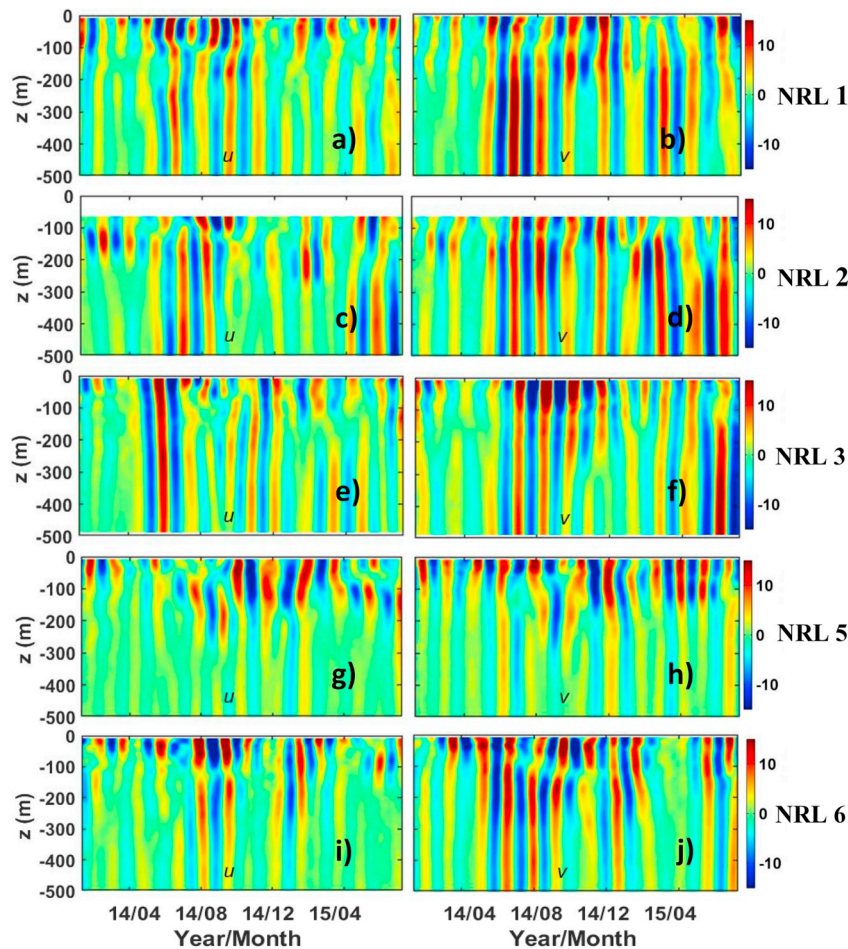
Fig. 4. Zonal and meridional intraseasonal currents (30–60 day filtered signals) at mooring locations. Units are in cm s^{-1}.

3. Detection of ISOs using mooring observations and satellite SSHA records

3.1. Intraseasonal oscillations (ISOs)

Modeling and analysis of SSHA show two dominant ISO bands in the equatorial IO: 30–60-day and 60-90-day (e.g. Han et al., 2001), and both 30–60-day (Figs. 3 and 4) and 60–90-day (not shown) bands were present in our case. In general, 60–90-day velocity fluctuations were limited to the upper 100 m, while 30–60-day velocity fluctuations extended to 500 m at all the mooring sites. *T* fluctuations as large as $\pm$ 1 °C were found in the thermocline where the vertical temperature gradient was strongest (Fig. 3), and they were smaller below 200 m, extending to about 400 m (Fig. 3).

For all moorings, the 30–60-day ISO velocities (obtained with a 5th order Butterworth filter) were as large as 14 cm s^{-1} in the upper 100 m, and were nearly uniform below 100 m depth (Fig. 4). We suspect that the higher velocities in the upper 100 m are due to contributions of the SLD and AE, which are strongest in the top 100 m with a residence time of ~30–60 days and velocities greater than 40 cm s^{-1}. In general, the 30–60-day ISOs appeared at the beginning of the 2014 summer monsoon, and lasted throughout the summer with nearly uniform magnitudes between ~120 and 500 m (limit of ADCPs measurements). The meridional velocity fluctuations below 120 m were about ± 10 cm s^{-1}, which were larger than the zonal component. After the summer 2014, the ISO velocity fluctuations gradually decayed into the winter.

The temporal variability of 30–60-day ISOs was further investigated by computing the depth-averaged kinetic energy (*KE*) in the depth range

(~120–500 m) where velocity fluctuations were nearly uniform. A 60-day running mean was also used to obtain a smooth time series. The averaged *KE* peaked during June–October 2014 when southwesterly winds were strongest (Fig. 5b). These oscillations were strongest at the southwestern edge of the mooring array (i.e. at NRL1), where *KE* was ~100 cm^2 s^{-2} $\approx$ 10 J m^{-3} and weakest at the eastern mooring NRL5 where KE was less than 20 cm^2 s^{-2}. For NRL2, NRL3 and NRL6, KE was $\approx$ 60 cm^2 s^{-2}. The *KE* averaged over the entire mooring array was about 20–40 cm^2 s^{-2} for June–October 2014. The intensification of KE on the western side of the mooring array coincided with the onset of the summer monsoon (Fig. 5a and b), along with the appearance of the SMC and two large mesoscale eddies (Fig. 2). Similarly, the depth-averaged temperature variance for the 30–60-day band, $\langle T'2 \rangle$ was computed by averaging between 90 m and 388 m in depth and applying a 60-day running mean in time (Fig. 5c). Like KE, $\langle T'2 \rangle$ also peaked during June–July 2014 just after the onset of the monsoon. The mean peak $\langle T'2 \rangle$ was ~0.9°C^2 and the averaged $\langle T'2 \rangle$ was ~0.42°C^2 over the mooring array. Temperature fluctuations (*T'*) can dominate density fluctuations of ISOs when the salinity contribution to density becomes insignificant, which occurs below 100 m, whereby the perturbation potential energy per unit volume becomes; α is the thermal expansion coefficient; ρ the sea water density; *g* is the gravitational acceleration; and $\partial \overline{T}/\partial z$ is the mean temperature gradient. Note that *PE* is not the available potential energy based on the difference between total potential energy and minimum total potential energy (e.g. equation (10) in Oort et al., 1989).

First for a given depth, $T'2 \left[\frac{dT}{dz} \right]^{-1}$ was evaluated and then was depth averaged between 90 m and 388 m to generate a time series of *PE* as shown in Fig. 5d. The time averaged *PE* for the May–October period is
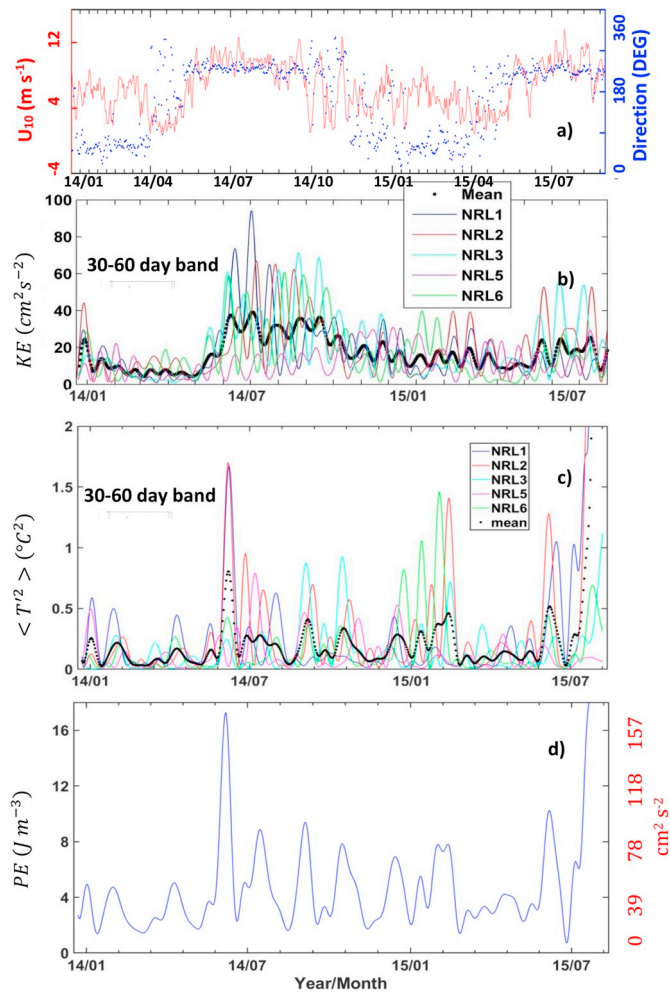
Fig. 5. (a) Direction (blue) and magnitude (red) of ECMWF reanalysis winds averaged over the six moorings location. (b) Depth averaged (120–500 m) oceanic kinetic energy for the 30–60 band at NRL1-6 along with the mean (back dots). (c) Depth averaged (90–388 m) oceanic temperature variance for the 30–60 day at NRL1-6 band along with the mean (back dots). (d) Depth-averaged (90–388 m) perturbation potential energy (PE) averaged for NRL1-6 in J m^{-3}. Right axis has units in cm^2 s^{-2} for comparison with *KE*. (For interpretation of the references to color in this figure legend, the reader is referred to the Web version of this article.)

about $5.3\,\mathrm{J\,m^{-3}}$ for $T'2\left[\frac{d\bar{T}}{dz}\right]^{-1} = 3.5\,^{\circ}\mathrm{C}$ m, for $\rho = 1020\,\mathrm{kg\,m^{-3}}$; and $\alpha = 3 \times 10^{-4}\,^{\circ}\mathrm{C}^{-1}$. This rough estimate of *PE* is comparable with the *KE* for the 30–60-day ISOs (Fig. 5b, d).

3.2. Spectral properties

To examine dominant frequency bands in the energy and momentum flux distributions, the power spectra of zonal velocity *u* (Φ_{UU}) and meridional velocity *v* (Φ_{VV}), and co-spectra of *u* and *v* (Φ_{UV}), were computed for all five moorings. Frequency-depth spectral plots were constructed by computing the frequency spectrum for a given depth using 20-month-long velocity records. Fig. 6 shows these plots for three moorings (NRL1, NRL2, and NRL6) that registered the highest values of perturbation *KE* (Fig. 5b). Compared to the power spectra of zonal velocity (Fig. 6a, b, c), the meridional velocity spectrum (Φ_{VV}) (Fig. 6d, e, f) exhibits a narrow-band spectral peak for the period 46–52 days (frequency ≈ 3 to 3.125×10^{-4} cph) which extends at least to 500 m in depth. Φ_{VV} shows high energy levels in the upper 100 m and is nearly uniform in the thermocline (120–500 m). The co-spectra Φ_{UV} (Fig. 6g, h,

i) also shows positive momentum flux for the 46–52-day ISO band in the thermocline especially for NRL1 and NRL2. The ISO fluxes peaked at 200 m depth (Fig. 6 g, h, i). However, the coherence between *u* and *v* was weak in the upper 100 m. Perhaps band-pass-filtered velocities could have been contaminated by eddy contributions as discussed before. For NRL6, high momentum fluxes were limited to 50–100 m depths.

Spectral properties were examined by constructing depth-averaged zonal (Φ_{UU}) and meridional (Φ_{VV}) velocity spectra over 120–500 m depth range (Fig. 7b and c). An identifiable spectral peak near 8×10^{-4} cph (or 52-day period) can be seen in the Φ_{VV} shown in Fig. 7c for NRL 1, NRL2 and NRL6, as was found in Fig. 6. Fig. 7a shows frequency spectra of zonal and meridional components of surface wind speed. The spectral peaks in wind partially overlap with the ISO velocity peaks. Spectral peaks discussed are significant at 95% (Jenkins and Watts, 1969). We will discuss correlations between wind and ISO in detail in Section 4.

Vertical profiles of kinetic energy at NRL1-6 were constructed by integrating Φ_{UU} and Φ_{VV} for the 30–60-day band encompassing spectral peaks shown in Figs. 6 and 7, where $KE = 0.5 \int_{\omega_1}^{\omega_2}(\Phi_{VV} + \Phi_{UU})d\omega$, and $\omega_1 = 1/60\,\mathrm{d^{-1}}$ and $\omega_2 = 1/30\,\mathrm{d^{-1}}$. The *KE* was 80–160 cm^2 s^{-2} near the surface, and decreased rapidly to about 40 cm^2 s^{-2} at 100 m (Fig. 8a). The near-surface *KE* for NRL3 and NRL6 was about 150–160 cm^2 s^{-2}, and for NRL1 and NRL5 was about 80–120 cm^2 s^{-2}. No information is given for NRL2 in the upper layer since data were available only below 64 m. Below 100 m, the *KE* varied between 10 and 40 cm^2 s^{-2} for all five mooring sites. As discussed before, we suspect that 30–60-day velocity fluctuations in the upper 100 m are likely to be contaminated by AE and SLD, thus registering high *KE* values in the upper 100 m compared to that below 100 m.

Vertical profiles of momentum flux, *uv* (Fig. 8b) were computed by integrating Φ_{UV} for the 30–60-day band, where $uv = \int_{\omega_1}^{\omega_2} \Phi_{UV}d\omega$. Positive values of *uv* were found for most of the mooring locations. Estimates of *uv* were as large as 30 cm^2 s^2 at 50 m for NRL6 and at 200 m for NRL2. The momentum flux averaged over the mooring array was about 5–10 cm^2 s^{-2}.

3.3. Propagation of ISO signals from satellite SSHA

Here we used the 0.25° spatial-resolution AVISO (Archiving, Validation and Interpretation of Satellite Oceanographic) data set https://www.aviso.altimetry.fr/en/data/products/sea-surface-height products/global/ssha.html. Time-longitude (Hovmöller) diagrams of 30–60-day band-pass-filtered SSHA along different latitudes (4°–8°N) for January 2013 to August 2015, are shown in Fig. 9. The slope of the Hovmöller diagram provides the phase speed of the propagating signal. Unlike the 120-day low passed SSHA (see Fig. 9 of Wijesekera et al., 2016b), the 30–60-day ISO signal was patchy in both space and time. At low latitudes (4° - 5°N) and away from Sri Lankan land mass, waves propagated westward from the eastern boundary of the BoB. Between May and October 2013, at 6.5°N, SSHAs of magnitudes $\sim \pm 4$ cm propagated westward, but close to the Sri Lanka coast near 82°E, slopes of Hovmöller plots changed with no clearly defined slopes. At 8°N, energy associated with the incoming wave was likely focused/reflected near the coast of Sri Lanka (~82°E). In July–August 2013, high values of SSHA $\sim \pm 8$ cm occupied the region over the mooring array (85.5°–87°E).

During 2014, weak signals of ±2 cm propagated from the eastern side of the BoB at latitudes 4°–5°N, and then intensified up to ±6 cm during July–August. SSHAs with a quasi-linear longitude-time slopes intensified at 6.5°N and 8°N over the mooring array in July–August and July–September, respectively. At 8°N and to the west of 86°E, the ISOs started moving westward in October 2014 (Fig. 9).

Two statistical analyses were conducted to evaluate the phase velocity of the westward propagating SSHAs. In the first, phase speeds were based on the slopes of time – longitude diagrams presented in Fig. 9. At each latitude, several sloping SSHAs were identified, and phase
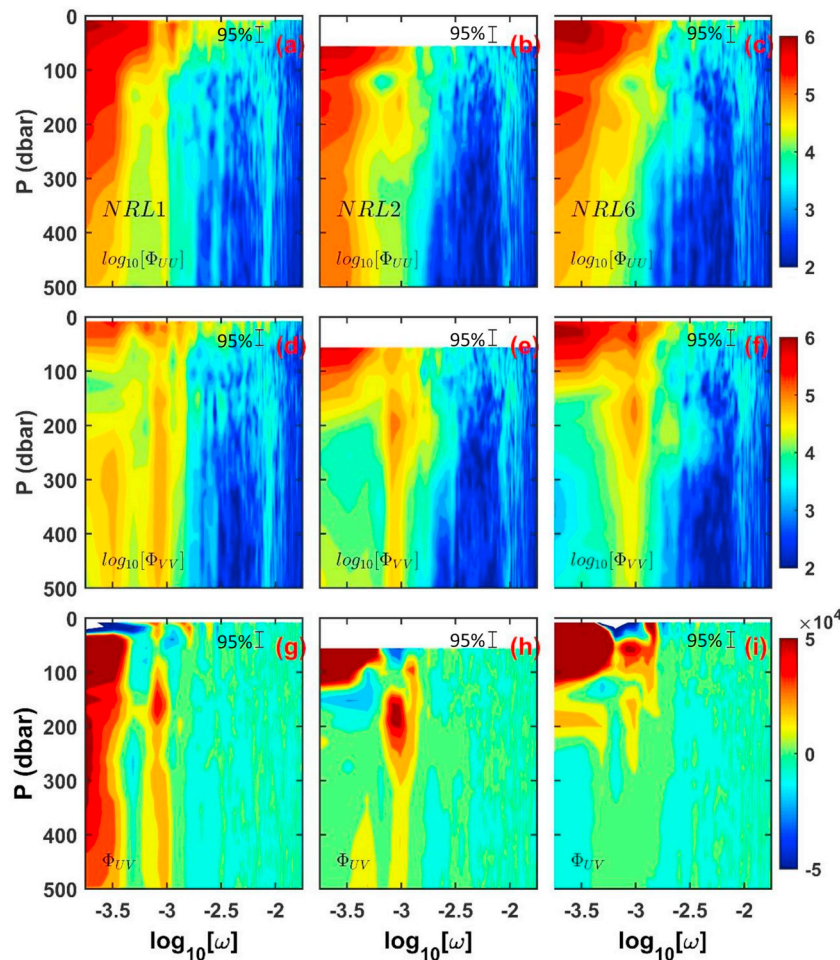
Fig. 6. Power spectra of zonal velocity (U), Φ_{UU} (top panels) and meridional velocity (V), Φ_{VV} (middle panels), and co-spectra of U and V, Φ_{UV} (bottom panels) at NRL1, NR2, and NRL6. Units are in cm^{2}s^2. The frequency ω is in cycles per hour (cph).

speeds were calculated and averaged over selected latitudinal intervals. The mean phase velocities (Fig. 10a) varied with latitude: from 0.43 m s^{-1} at 4°N to 0.17 m s^{-1} at 8°N. These values are consistent with the characteristics of Rossby waves, and are in agreement with the Rossby wave phase speeds described by Girishkumar et al. (2011). Specifically, they found that westward phase speeds of 40-100 day band-pass filtered SSHA signals at 8°N were between 0.21 and 0.23 m s^{-1}. The second method is an autocorrelation-function approach that utilizes two time series from 1/1/2013 to 08/15/2015. The first time series was taken at the starting point of a westward propagating SSHA and the second time series was taken at the end point of the SSHA. In general, both methods produced similar results (Table 1). At 4°N, both methods provided similar mean phase speeds, while at 5°N, the phase-velocity difference was ~0.1 m s^{-1}. At 6.5° − 8°N the difference between the two methods was as small as 0.02 m s^{-1}.

The estimated phase speeds from both methods are plotted as a function of latitude along with the previously published observations and the theoretical first-mode baroclinic Rossby-wave speeds from Chelton and Schlax (1996) (Fig. 10b). They reported that the phase speed of baroclinic Rossby waves above 10°N and below 10°S are systematically greater than those predicted by the standard theory for freely propagating linear, first-mode baroclinic Rossby waves. For the equatorial band between 10°N and 10°S it also departs from the standard theory (Fig. 10b). The estimated phase speeds are within the phase speeds of 1st and 2nd modes of baroclinic Rossby Waves (e.g. between 25 and 40 m s^{-1} and between 10 and 20 m s^{-1} for 1st and 2nd mode, respectively; see Fig. 1 of Subrahmanyam et al., 2001) but they are

slightly larger than the mode 2 wave speeds.

In summary, the combined moored velocity measurements and SSHA records indicate westward propagating waves of period ~46–52 days and phase speeds that are slightly above the mode-2 baroclinic Rossby waves. For a wave period of 49 days (Fig. 7c) and a westward zonal phase speed of $c = 0.17$–0.43 m s^{-1} (Fig. 10a), the zonal wavelength (λ_x) varies between 700 and 1200 km. The moored velocity records showed that the KE of the 30–60- day ISO band was strongest in the upper 100 m and was nearly uniform below 100 m. Furthermore, the moored records showed the existence of near-uniform, positive momentum flux below 100 m when the ISO signal was strong. On the average, these waves carried westward momentum flux of $F_{uv} \sim 8$ cm^2 s^{-2} and wave energy of $E_H \sim 20$ cm^2 s^{-2} in the thermocline (Fig. 8).

4. Local winds role on the ISOs formation

The power spectra of surface winds, and currents in the thermocline over the mooring array (Fig. 7 a, b, c) revealed several intraseasonal peaks, including a well-defined peak in the frequency spectra of winds between 23 and 26 days (~1.6–1.8 × 10^{-3} cph; Fig. 7a), and a less pronounced peak in the zonal wind spectrum at a 52–59-day period (black rectangle in Fig. 7a) that marginally coincides with the spectral peak in the ISO velocity spectra at a 48-52-day period (Fig. 7b and c). A recent study by Cheng et al. (2013) suggests that the local wind contribution to 30–60-day SSH variability east of Sri Lanka is about 20%. Girishkumar et al. (2013) reports that a 30–70-day thermocline variability is affected by interior Ekman pumping over the BoB, remote
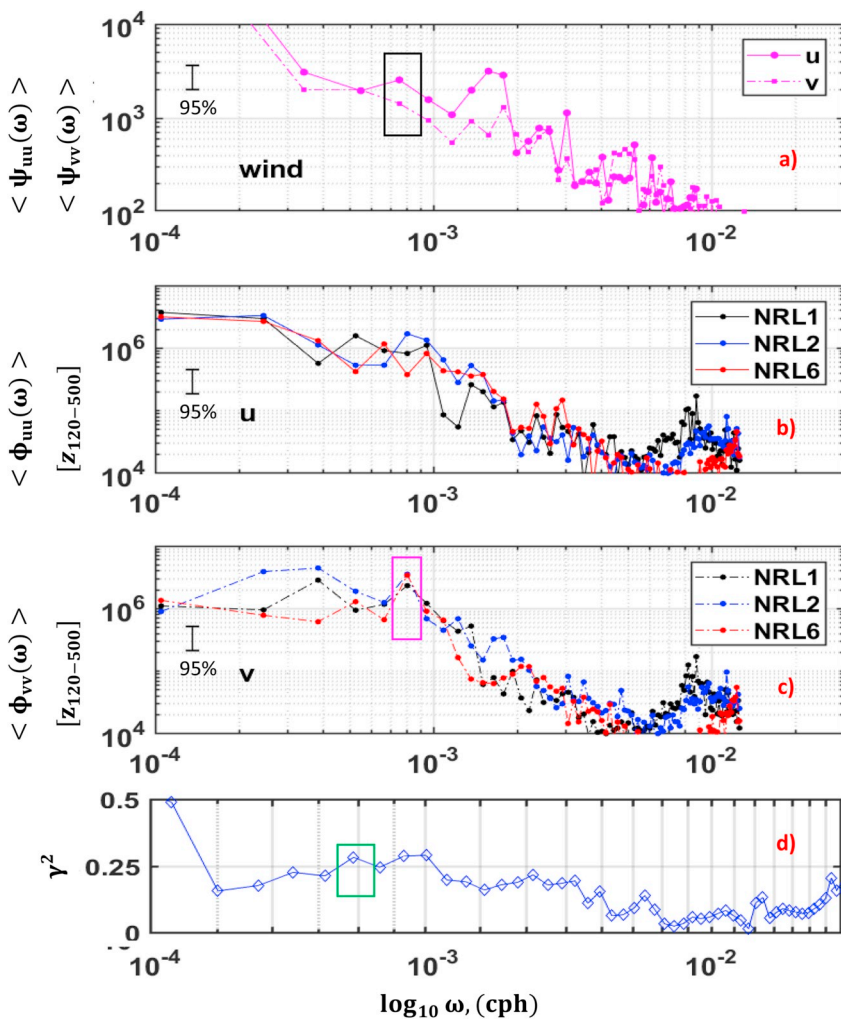
Fig. 7. Zonal (solid line) and meridional (dashed line) spectra for ECMWF wind in m^2s^{-2} cph^{-1} averaged for the six moorings location. Significant peak (at 95%) is indicated by black rectangular (a). Depth-averaged zonal velocity spectra in cm^2s^{-2} cph^{-1} computed for NRL1 (black line), NRL2 (blue line), NRL6 (red line). Spectra were averaged between 120 m and 500 m (b). Depth-averaged meridional velocity spectra in cm^2s^{-2} cph^{-1} computed for NRL1 (black line), NRL2 (blue line), NRL6 (red line). Spectra were averaged between 120 m and 500 m. Significant peak (at 95%) is indicated by magenta rectangular (c). Coherence squared between wind stress and moored velocities (NRL 1,2,6) averaged between 120 and 500 m. Green box indicates coherence squared at 52-day period. The 95% confidence limit for γ^2 is ~0.09. Frequency ω is in cph (d). (For interpretation of the references to color in this figure legend, the reader is referred to the Web version of this article.)
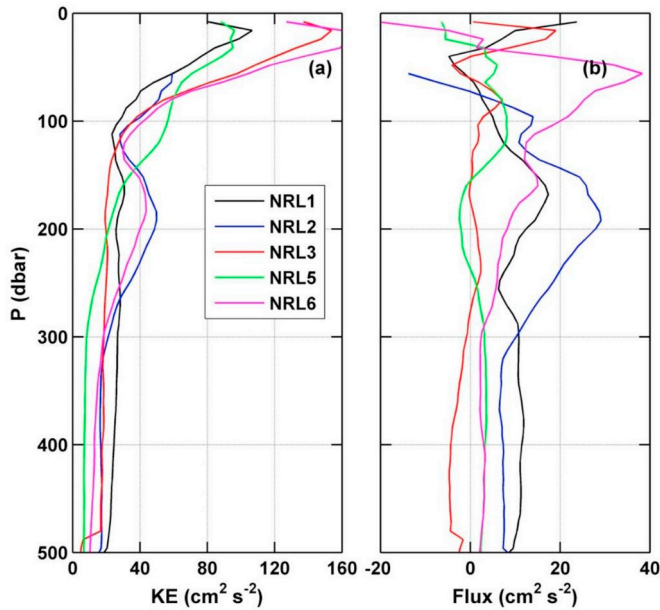

Fig. 8. Time averaged kinetic energy (left) and momentum flux <uv> (right) for 30–60 day band estimated from moored velocities and momentum flux spectra, respectively.

forcing of zonal winds at the equatorial IO, and alongshore winds in the eastern boundary of the BoB. To examine impacts of local winds on ISO variability, the coherence, γ, between ocean currents and the surface wind field was calculated using in-situ velocity and ECMWF wind fields, where

$$\gamma^2 = \frac{|S_{\tau q}|^2}{S_{\tau\tau} \, S_{qq}}. \tag{1}$$

$S_{\tau q}$ is the covariance between rotary velocity component q and the rotary shear stress τ as a function of frequency (Mooers, 1973), and S_{qq} and $S_{\tau\tau}$ are the autospectral power density function of q and τ, respectively. One can interpret γ^2 as the percentage of variance of q that is ascribable to linear forcing by τ (Elipot, 2006). The coherence squared (Fig. 7d) was computed between the ECMWF wind stress and the depth-averaged velocity vectors between 120 and 500 m. The squared coherence is 0.25 ± 0.09 for the 52-day period (green rectangular in Fig. 7d). The 95% confidence limit for the γ^2 estimate is 0.09 (Thomson and Emery, 2014). Since γ^2 measures the fraction of the currents directly related to local wind forcing, these results imply that winds having 52–59-day periods could account for roughly 25% of the ISO variability. The estimated γ^2 for the summer of 2014 is consistent with the earlier findings of Cheng et al. (2013) that local wind forcing is not the main mechanism for generating ISOs in the southern BoB. The SSHA analysis (Fig. 9) indicates that the westward propagating ISOs are likely generated at the eastern boundary (e.g. Girishkumar et al., 2013).
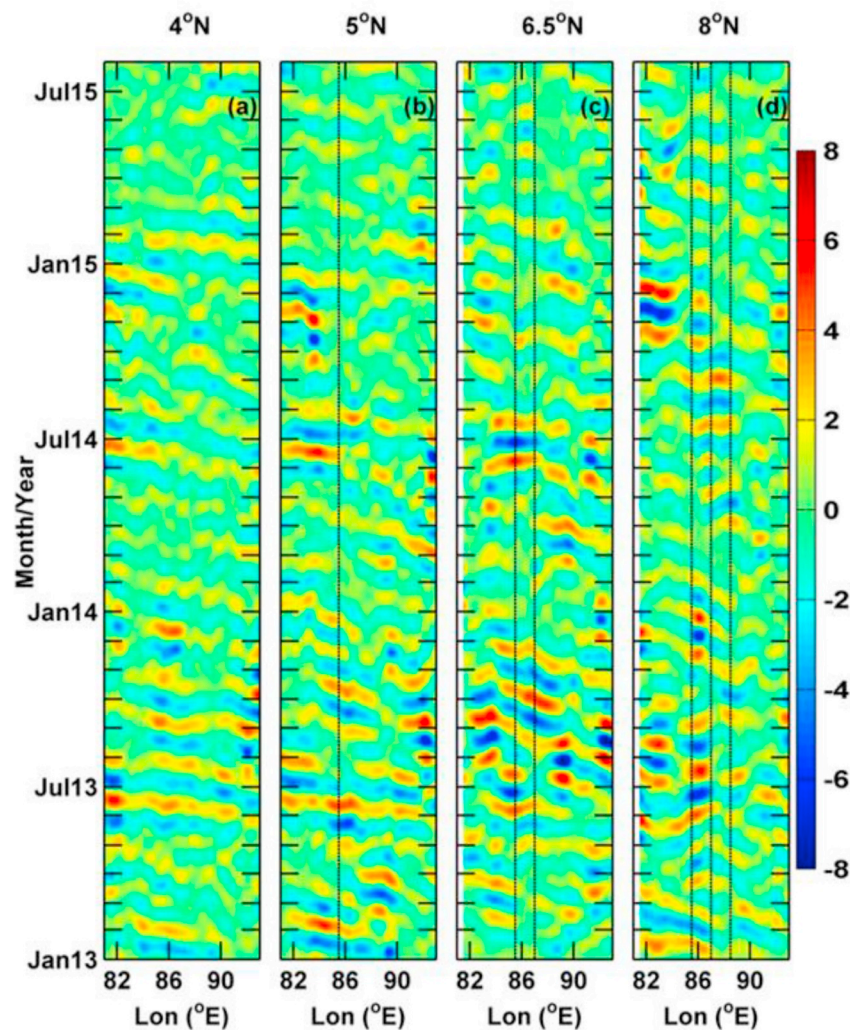
Fig. 9. Longitude-Time plots of 30-60 day band-passed filtered SSH anomalies at 4 °N (left), 5 °N, 6.5 °N and 8 °N (right). SSHA is from AVISO data products (2013/1/1–2015/8/15). Dash lines indicate location of moorings. Units of SSHA are in cm.
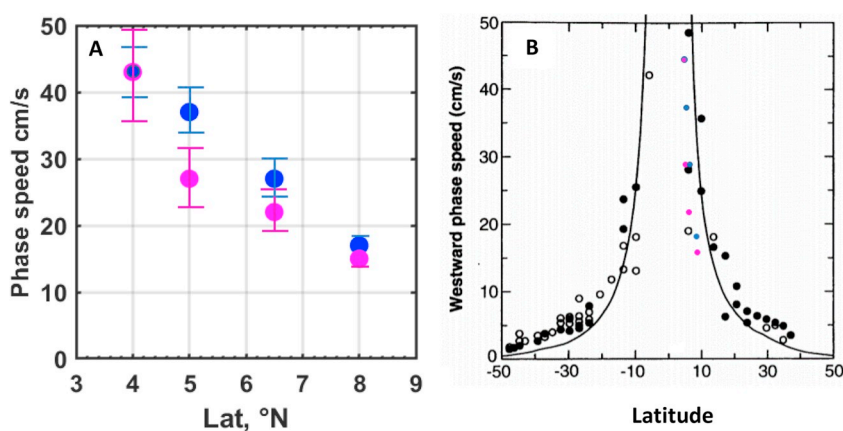

Fig. 10. Left: Mean phase speeds based on the slope of the Hovmöller diagrams for the 30–60 day band pass filter SSHA dataset from 12/1/2013 to 8/15/2015 (blue circles). Magenta circles: same as blue circles, but based on the autocorrelation function. Standard mean errors for each mean phase speed are identified by colored bars Right: Westward propagating sea level signals estimated from TOPEX/POSEIDON altimeter observations from Chelton and Schlax (1996). Solid (open) circles correspond to Pacific (Atlantic and Indian) ocean estimates. Solid lines represent the global average latitudinal variation of the phase speed predicted by the standard theory for extratropical freely propagating, nondispersive, linear, first-mode baroclinic Rossby waves. Blue and magenta circles are the velocities represented in Fig. 10a. (For interpretation of the references to color in this figure legend, the reader is referred to the Web version of this article.)

5. Impacts of ISOs on the background flow and thermocline

In the following we examine the impact of ISOs on energetics, wave momentum and heat fluxes in the thermocline by combining in-situ current velocity and temperature records, thus complementing previous studies of Rossby-wave and mean (background) flow interactions in the southern BoB based on XBT/CTD observations, model simulations and satellite products (e.g. Vinayachandran et al., 1999; Cheng et al., 2013; Girishkumar et al., 2013; Rath et al., 2017). We follow the analysis of Weisberg and Weingartner (1988), which used temperature and velocity time series from current meter moorings to examine instability waves and their role in the near-surface circulation of the equatorial

Table 1

Phase speed calculated from Hovmöller diagrams (slope) and from autocorrelation function (correlation) for 30–60 day SSHA data.

	slope	correlation	slope	correlation	slope	correlation	slope	correlation
	4N	**4N**	**5N**	**5N**	**6.5N**	**6.5N**	**8N**	**8N**
	m/s	*m/s*	*m/s*	*m/s*	*m/s*	*m/s*	*m/s*	*m/s*
	0.5264	0.2174	0.4799	0.3339	0.2641	0.2735	0.1995	0.1509
	0.4606	0.2174	0.32	0.2167	0.2321	0.2735	0.1421	0.1452
	0.4929	0.5696	0.4114	0.4799	0.2593	0.1565	0.1864	0.1744
	0.2403	0.3738	0.3927	0.3756	0.3942	0.1064	0.1777	0.1631
	0.4216	0.6942	0.2593	0.1249	0.3058	0.2936	0.1561	0.1407
	0.3595	0.2377	0.3942	0.2453	0.1937	0.217	0.1663	0.1421
	0.5006	0.6942	0.3058	0.1249				
			0.1937					
Mean Velocity	**0.43**	**0.43**	**0.37**	**0.27**	**0.27**	**0.22**	**0.17**	**0.15**

Atlantic Ocean. Our data sets were first averaged every 24 h and then a 30–60-day band-pass filter was applied before computing energetics and fluxes for 60-day subsampled data sets.

5.1. Horizontal wave momentum flux

Power spectra of the meridional velocity component showed a well-defined peak in the thermocline centered upon a 52-day period (Fig. 7c). The time series of *KE* of the 30–60-day band shows the ISO appeared in July 2014 and lasted throughout the summer of 2014 (Fig. 5b).

Time-depth series of horizontal momentum flux *uv* were estimated by computing covariances between *u* and *v* components for 60-day subsampled data records for each mooring site. The horizontal momentum flux, $-uv$, computed at NRL2 is shown in Fig. 11a. *uv* was about $\sim 50 \times 10^{-4} \, m^2 \, s^{-2}$ between 100 m and 500 m, and had a similar seasonal modulation as the perturbation kinetic energy. As we discussed above, the time-domain band-passed filter does not always remove eddies of resident time scales ~30 days, and therefore the upper 100-m
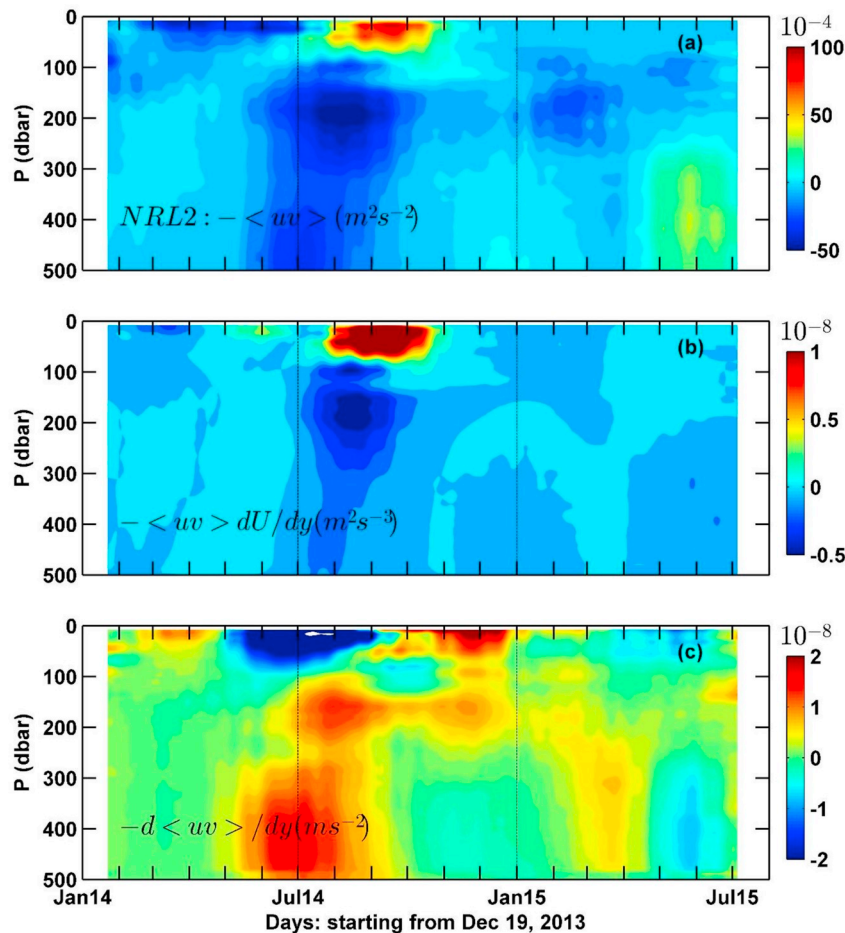

Fig. 11. Time-depth plot of momentum flux (a). Production/destruction term (b), and momentum flux divergence (c). Moored velocities are 30-60 day band pass filtered.

ISO velocities are contaminated by eddies. In the upper 100 m, uv was negative $\sim -(70-100) \times 10^{-4}\,\mathrm{m^2\,s^{-2}}$ from August through the middle part of October 2014, when a large anticyclonic eddy occupied in the mooring array (see Fig. 10b of Wijesekera et al., 2016b).

5.2. Deformation work/production term

The processes that control the growth and decay of the perturbation kinetic energy can be studied by examining the terms in the perturbation kinetic-energy equation, for example, using the form used in studies of ocean energetics (e.g. Brooks and Niiler, 1977; Szabo and Weatherly, 1978; Rossby, 1987; Weisberg and Weingartner, 1988). We were unable to compute all relevant terms due to limitations of our moored observations, and therefore focus on the deformation work (also called the barotropic production term) that represents the energy conversion by Reynolds stresses acting on the mean flow. Both, zonal and meridional terms, $uv\frac{dU}{dy}$ and $uv\frac{dV}{dx}$, were computed, but $uv\frac{dV}{dx}$ was found to be small.

The deformation term, $-uv\frac{dU}{dy}$, at NRL2 was computed by combining NRL1, 2, and 3 for 60 day subsamples, similar to the momentum-flux estimates (Fig. 11b). Here U was obtained by applying a 60-day running mean to daily-averaged moored velocity records after applying a 120-day low-pass filter, and $\frac{dU}{dy}$ was estimated by finite differencing U currents at NRL1 and NRL3. The deformation term shows negative shear production, i.e., $-uv\frac{dU}{dy} < 0$ (Fig. 11b), in the thermocline below 100 m during July–October 2014, when the ISOs were strong (Fig. 4), suggesting that the mean kinetic energy was increased at the expense of the ISO band at a rate of about $0.5 \times 10^{-8}\,\mathrm{m^2\,s^{-2}}$. Therefore, it is unlikely that barotropic instabilities lead to generation of ISOs.

In the upper 100 m, however, during August through mid-October 2014, the production term was positive, $\sim 0.3-1 \times 10^{-8}\,\mathrm{m^2\,s^{-3}}$, which partly coincided with the presence of the large AE eddy in the mooring area (Wijesekera et al., 2016a; Pirro et al., 2020). Positive values of $-uv\frac{dU}{dy}$ suggest that the anticyclonic eddy may gain energy by at the expense of the SMC through barotropic instability. For example, the mean kinetic-energy loss at a rate of $1 \times 10^{-8}\,\mathrm{m^2\,s^{-3}}$ for a period of 60 days could enable the anticyclonic eddy to gain eddy kinetic energy of about $5 \times 10^{-2}\,\mathrm{m^2\,s^{-2}}$, corresponding to a gain of velocity $\sim 15\,\mathrm{cm\,s^{-1}}$.

5.3. Wave momentum flux divergence and acceleration of the background flow

Waves propagating across meridionally and vertically sheared zonal currents may alter the momentum balance of the mean zonal flow (Weisberg and Weingartner, 1988), the conditions for the occurrence of which were first addressed by Elliasen and Palm (EP) (1960) in the context of two-dimensional nonrotating internal gravity waves interacting with vertically-sheared mean currents. Subsequently, Charney and Drazin (1961) extended these techniques for eddy transports associated with vertically-propagating mid-latitude atmospheric planetary waves, and McPhaden et al. (1986) to examine the interaction of baroclinic equatorial Kelvin waves with sheared zonal currents in the ocean. The zonal momentum equation as a function of the EP-flux vector can be summarized in the following equation:

$$U_t = -uv_y + fv\rho_z'/\rho_z = \nabla \cdot \boldsymbol{F}, \tag{2}$$

where U is the mean zonal current, ρ the mean density; f the inertial frequency; u, and v the perturbation zonal and meridional velocities, respectively, and ρ' the perturbation density. Subscripts y and z denote partial derivatives of y and z, respectively (see Appendix A for details).

To evaluate the density flux $v\rho'$ in eq [2], a time-depth series of density is needed, but the conductivity (salinity) measurements were sparse on the mooring lines due to the limited CTD sensor coverage. Therefore, we used temperature measurements, considering the fact that

density in the thermocline was dominated by the temperature. As a result, the meridional flux of density in eq [2] could be expressed in terms of meridional heat flux and background temperature gradient:

$$U_t = -uv_y + fvT_z'/T_z = \nabla \cdot \boldsymbol{F}. \tag{3}$$

The meridional fluxes of zonal momentum $-uv$ and heat flux vT' were estimated for each 60-day subsampled data record by computing covariance of u and v, and v and T', respectively. The baroclinic term, fvT_z'/T_z, was estimated at NRL1, NRL2, NRL3. We noted that the meridional momentum-flux divergence is significantly larger than the baroclinic flux term, fvT_z'/T_z. As a result, eq [3] can be written as

$$\frac{\partial U}{\partial t} \approx -\frac{\partial uv}{\partial y} = v\xi, \tag{4}$$

where $v\xi$ is the meridional vorticity flux (Pedlosky, 1987). As for the deformation term, the wave-momentum flux divergence was computed by combining NRL1, 2, and 3 (Fig. 11c). The momentum-flux divergence, $-\frac{\partial uv}{\partial y}$, was positive in the thermocline below 100 m, during May–August whence the ISO was strongest. Below 100 m, $\frac{-\partial <uv>}{\partial y}$ is of order $10^{-8}\,\mathrm{m\,s^{-2}}$. For a period of 60 days, the meridional wave-flux divergence can increase the background current as much as $5\,\mathrm{cm\,s^{-1}}$, which is about 25% of the background flow. Note that the zonal current below 100 m was $\sim 15-20\,\mathrm{cm\,s^{-1}}$ (Fig. 2). The analysis suggests that $\frac{-\partial <uv>}{\partial y}$ is significant for transferring wave momentum to the currents in the thermocline.

5.4. Heat flux divergence and cooling of the thermocline

Zonal and meridional heat-flux divergences were estimated by computing covariance of u and T', and v and T' at the mooring sites for every 60-day time period. The meridional divergence was computed for NRL1 and NRL3 using the same procedure as the wave momentum-flux divergence, which was stronger than the zonal heat-flux divergence. The estimated heat fluxes at NRL1, 2, and 3 along with the meridional divergence of heat fluxes are shown in Fig. 12. The meridional heat-flux divergence, $\frac{-\partial <vT>}{\partial y}$, was negative in the thermocline and penetrated deep during May–October when summertime ISOs were the strongest (Fig. 12). During the passage of ISOs, the thermocline cools at a rate of about $-10^{-7}\,^{\circ}\mathrm{C\,s^{-1}}$ (Fig. 12d), which can generate cooling of about $0.5\,^{\circ}\mathrm{C}$ for a period of 60 days. This substantial amount of cooling in the thermocline can alter the upper-ocean heat budget and sea-surface temperature, which impacts the monsoon variability over the BoB (e.g. Vecchi and Harrison, 2004; Izumo et al., 2008).

6. Summary and conclusions

Temperature and current time series from five long-term moorings deployed in the southern BoB during Air–Sea Interactions in Northern Indian Ocean (ASIRI) field campaigns were used to present evidence of 30–60-day ISOs in the thermocline and to quantify the impact of the intraseasonal oscillations (ISOs) on the eastward background flow of the SMC and on the thermocline. To our knowledge, this is the first time that such long-term multiple mooring records have been taken in the southern BoB. The methodology followed the previous work of Weisberg and Weingartner (1988) on instability waves and their role in near-surface circulation of the equatorial Atlantic.

Currents and hydrographic measurements collected from December 2013 to August 2015 over the upper 500 m in the region of (85.5°–88.5°E) and (5°–8°N) detected 30–60- day ISOs at the beginning of the 2014 summer monsoon. The u and v fluctuations near the surface (less than 100 m in depth) reached strong velocities of $\sim \pm 14\,\mathrm{cm\,s^{-1}}$ and were strikingly nearly uniform between $\sim 120\,\mathrm{m}$ and 500 m (ADCP-measurements limit) with a magnitude of 4-14 cm s^{-1} (Fig. 4). Stronger
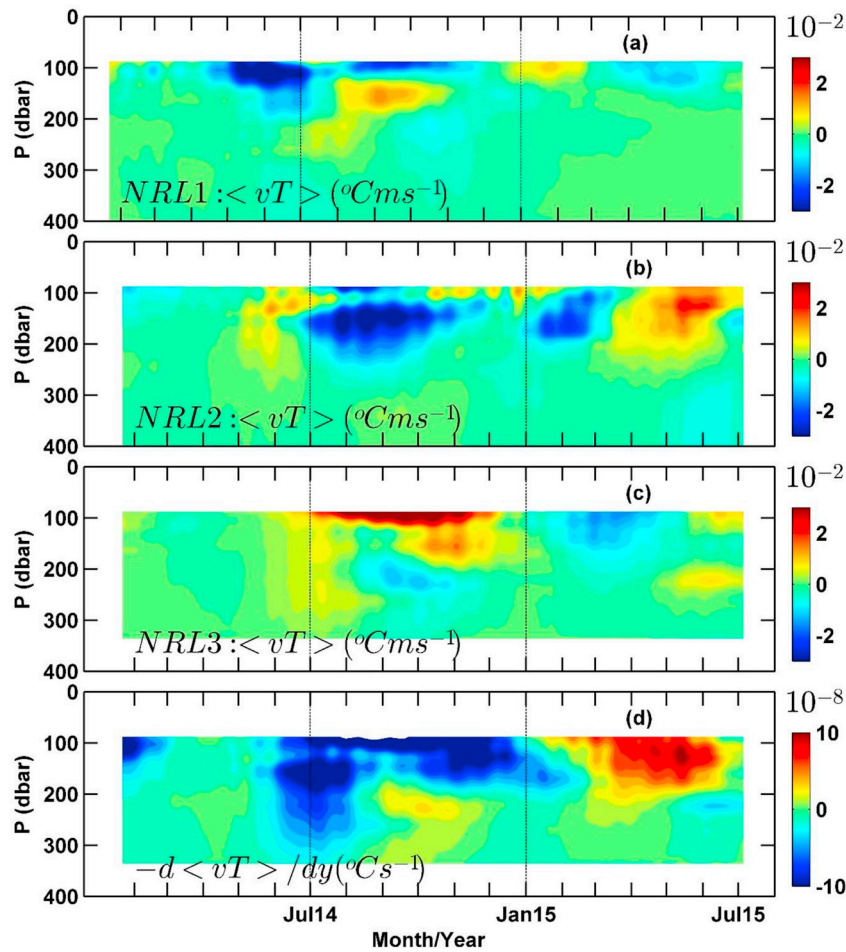
Fig. 12. Time-depth sections of meridional heat flux for the 30–60 day band, NRL1(a), NRL2(b), and NRL3(c). Flux divergence computed by combining NRL1-3 (d).

oscillations in the mixed layer (less than 100 m in depth) may be due to eddies (e.g. an AE and the SLD) that have residence periods of 38–48 days and penetrate up to ~100 m of depth (Pirro et al.,2020). In general, at lower latitudes (NRL1, NRL2 and NRL6), the meridional v fluctuations in the thermocline were stronger than the zonal ones.

Power spectra of meridional velocity, Φ_{VV}, computed at NRL1, NRL2 and NR6 at different depths exhibited a clear narrow-band spectral peak with a period of 46-52 days (Fig. 6d, e, f), and the results were similar for the depth-averaged (120–500 m) meridional spectra (Fig. 7c). Even though 30–60-day kinetic energy, temperature variance, and perturbation potential energy averaged over the thermocline peaked during June–October 2014 (Fig. 5b, c, d) when southwesterly winds were strongest (Fig. 5a), local wind accounted for only ~25% of the oceanic variability observed at the mooring locations, which is consistent with Cheng et al. (2013). Therefore, a different formation mechanism, possibly the westward-propagating Rossby waves generated at the eastern boundary of the BoB due to reflection of equatorial Kelvin waves (Wyrtki, 1973), is responsible for the observed 30–60-day ISOs during the 2014 summer. Previous studies (Vinayachandran and Yamagata, 1998; Nagura and McPhaden, 2010; Chen, 2015; among others) show that reflected Rossby waves reach the central-eastern BoB during July–August, thus impacting the ocean circulation in that region. Hovmöller diagrams indeed confirm that in general 30–60-day signals propagate westward from the eastern boundary. The 30–60-day band-passed sea-surface-height anomalies propagated westward with phase speeds of 0.17 m s^{-1} at 8°N and 0.43 m s^{-1} at 4°N, which are between the calculated phase-speed ranges of mode-1 and mode-2 linear baroclinic Rossby waves.

The non-local generation of the ISOs is also supported by negative

values of the deformation/production term, $-uv\frac{dU}{dy}$ ($\sim$-0.5 × 10^{-8} m^2 s^{-2}, Fig. 11b) at NRL2 during July–October 2014. Inspection of the phase speed, period, wavelength, propagation direction, and lack of correlation with local winds lead us to suggest that 30–60 days ISOs are radiating from the eastern boundary.

It is known that the mass of water built up at the Sumatra coast upon the impinging of equatorial Kelvin waves (typically in May) slowly disperses over the following two months via Rossby waves (Wyrtki, 1973). Vinayachandran et al. (1999) used an ocean general circulation model and geostrophic currents derived from altimeter data to show that the eastward branch of the SMC intensifies when a westward propagating Rossby wave radiating from the Sumatra coast reaches 85°E south of Sri Lanka. Energetics based on satellite QSCAT data by Cheng et al. (2013) indicated that during the summer (June–August) the barotropic instability plays an important role in the western BoB. Accordingly, in June, eddy energy transfers to the SMC and accelerates the mean current, and during July–August the instability of the SMC converts mean energy to eddy energy. Modeling studies of Rath et al. (2017) show that the intensification of the SMC occurs in mid-June. Our analysis suggests that the background flow acceleration/deceleration may occur due to the divergence of the wave-momentum-flux, $\frac{-\partial <uv>}{\partial y}$, associated with 30–60-day ISOs (Fig. 11c). In the upper layer, the strongest barotropic instability occurred in August (when the AE was strong), which is qualitatively consistent with the numerical simulations of Cheng et al. (2013). In the thermocline, positive values of momentum-flux divergence ($\sim$10^{-8} m s^{-2}) registered from June to August 2014 suggest an increment of the background flow equal to ~ 5 cm s^{-1} for a period of 60 days. This corresponds to about 25% of the averaged velocity magnitude

observed over the same period below 100 m depth by Wijesekera et al. (2016b).

Negative values of the meridional-heat-flux divergence (Fig. 12d) evaluated for June–August 2014 suggest cooling of the thermocline by ~0.5 °C during the passage of 30–60-day ISOs. This might impact the upper-ocean heat content, entrainment flux at the base of the mixed layer, and the sea-surface temperature associated with ISO time scales, which in turn may impact monsoon variability over the BoB (Vecchi and Harrison, 2004; Izumo et al., 2008). The observations and inferences made during this study are expected to provide guidance for future long-term mooring deployments and science planning for ISO studies.

APPENDIX A

The conditions under which waves interact with a zonal current were first addressed by Elliesen and Palm, (1960) for the case of two-dimensional, nonrotating, internal gravity waves in a vertically-sheared current. Charney and Drazin (1961) extended this work to quantify eddy transports of heat and momentum in vertically propagating atmospheric waves in mid-latitudes, and derived the so called "nonacceleration" or "Charney-Drazin" theorem. Holton (1974) and Andrews and McIntyre (1976) extended Charney and Drazin's results to the equatorial β - plane. McPhaden et al. (1986) applied similar concepts to the ocean to study the interaction of baroclinic equatorial Kelvin waves with sheared zonal currents. Weisberg and Weingartner (1988) applied methods of Elliesen and Palm, (1960) and Charney and Drazin (1961) to study instability waves in the equatorial Atlantic Ocean, and in Section 5 we adopted Weisberg and Weingartner methodology, a brief summary of which is given below.

The sheared zonal flow, U, is in thermal wind balance and the meridional flow, V, is in geostrophic balance. Zonal averages are taken over a latitude circle, over a zonally-bounded basin with cyclic boundary conditions or over an unbounded domain in which the disturbances are evanescent. Under these conditions, terms differentiable with respect to longitude vanish as does the zonally-averaged V. Then the zonally-averaged zonal momentum, heat, and continuity equations become:

$$U_t = -f\tilde{v} = -(uv)_y, \tag{A1}$$

$$\rho_t + \tilde{w}\rho_y = -(u\rho')_y \tag{A2}$$

$$\tilde{v}_y + \tilde{w}_z = 0, \tag{A3}$$

where ρ', u, and v are departures from zonal averages, f the Coriolis parameter, and the derivatives are indicated by subscripts. If $U_t = 0$, and $\rho_t = 0$, continuity is satisfied with $\tilde{v} = [(v\rho')z / \rho_z]$ and $\tilde{w} = -[(v\rho')y / \rho_z]$. Substituting the expression for $\tilde{v}$ obtained from continuity equation, [A1] can be rewritten as:

$$U_t = -(uv)_y + f(v\rho')_z / \rho_z = \nabla \cdot \mathbf{F}, \tag{A4}$$

where $\mathbf{F}$ is the vector, $-uv\mathbf{j} + f(v\rho')/\rho_z \mathbf{k}$, which lies in the meridional plane, and is defined as the Eliassen-Palm or EP-flux vector.

Appendix B. Supplementary data

Supplementary data to this article can be found online at https://doi.org/10.1016/j.dsr2.2019.104718.

References

Andrews, D.G., McIntyre, M.E., 1976. Planetary waves in horizontal and vertical shears: the generalized Eliassen-Palm relation and mean zonal acceleration. J. Atmos. Sci. 33, 2031–2048.

Brooks, I.H., Niiler, P.P., 1977. Energetics of the Florida current. J. Mar. Res. 35, 163–191.

Charney, J.G., Drazin, P.G., 1961. Propagation of planetary-scale disturbances from the lower into the upper atmosphere. J. Geophys. Res. 66 (1), 83–109.

Chelton, D.B., Schlax, M.G., 1996. Global observations of oceanic Rossby waves. Science 272 (5259), 234–238.

Chen, Gengxin, et al., 2015. Seasonal-to-Interannual time-scale dynamics of the equatorial undercurrent in the Indian ocean. J. Phys. Oceanogr. 45 (6), 1532–1553.

Cheng, X., Xie, S.P., McCreary, J.P., Qi, Y., Du, Y., 2013. Intraseasonal variability of sea surface height in the Bay of Bengal. J. Geophys. Res. Oceans 118 (2), 816–830.

Clarke, A.J., Liu, X., 1993. Observations and dynamics of semiannual and annual sea levels near the eastern equatorial Indian Ocean boundary. J. Phys. Oceanogr. 23 (2), 386–399.

Cox, M.D., 1970. A mathematical model of the Indian Ocean. Deep Sea Res. 17, 47–75. Pergamon Press. Printed in Great Britain.

Elipot, S., 2006. Spectral characterization of Ekman velocities in the Southern Ocean based on surface drifter trajectories. UC San Diego. ProQuest ID: umi-ucsd-1392. Merritt ID: ark:/20775/bb6280737k. Retrieved from. https://escholarship.org/uc/item/2pp898fv.

Elliesen, A., Palm, E., 1960. On the Transfer of Energy in stationary mountain waves. Geophys. Publ. 22, 1–23.

Fu, L.-L., 2007. Intraseasonal variability of the equatorial Indian Ocean observed from sea surface height, wind, and temperature data. J. Phys. Oceanogr. 37 (2), 188–202. https://doi.org/10.1175/JPO3006.1.

Girishkumar, M.S., Ravichandran, M., McPhaden, M.J., Rao, R.R., 2011. Intraseasonal variability in barrier layer thickness in the south central Bay of Bengal. J. Geophys. Res. 116 https://doi.org/10.1029/2010JC006657. C03009.

Girishkumar, M.S., Ravichandran, M., Han, W., 2013. Observed intraseasonal thermocline variability in the Bay of Bengal. J. Geophys. Res. Oceans 118 (7), 3336–3349.

Goswami, B.N., 2005. South Asian summer monsoon. In: Lau, K., Waliser, D. (Eds.), Intraseasonal Variability of the Atmosphere-Ocean Climate System. Praxis Publishing, pp. 19–61.

Han, W., 2005. Origins and dynamics of the 90-day and 30–60-day variations in the equatorial Indian ocean. J. Phys. Oceanogr. 35, 708–728. https://doi.org/10.1175/JPO2725.1.

Han, W., McCreary, J.P., Anderson, D.L.T., Mariano, A.J., 1999. Dynamics of the eastward surface jets in the equatorial Indian Ocean. J. Phys. Oceanogr. 29, 2191–2209. https://doi.org/10.1175/1520-0485(1999)029,2191:DOTESJ.2.0.CO;2.

Han, W., Lawrence, D.M., Webster, P.J., 2001. Dynamical response of equatorial Indian Ocean to intraseasonal winds: zonal flow. Geophys. Res. Lett. 28, 4215–4218.

Holton, J.R., 1974. Forcing of mean flows by stationary waves. J. Atmos. Sci. 31, 942–945.

Iskandar, I., Mardiansyah, W., Masumoto, Y., Yamagata, T., 2005. Intraseasonal Kelvin waves along the southern coast of Sumatra and java. J. Geophys. Res. 110 https://doi.org/10.1029/2004JC002508. C04013.

Iskandar, I., Tozuka, T., Sasaki, H., Masumoto, Y., Yamagata, T., 2006. Intraseasonal variations of surface and subsurface currents off Java as simulated in a high-resolution ocean general circulation model. J. Geophys. Res. 111 https://doi.org/10.1029/2006JC003486. C12015.

Izumo, T., de Boyer Montegut, C., Luo, J.-J., Behera, S.K., Masson, S., Yamagata, T., 2008. The role of the western Arabian Sea upwelling in Indian monsoon rainfall variability. Climate 21, 5603–5623.

Jenkins, G.M., Watts, D.G., 1969. Spectral Analysis and its Applications. Holden-Day Series in Time Series Analysis. Holden-Day, London, 1969.

Jochum, M., Murtugudde, R., 2005. Internal variability of Indian ocean SST. J. Clim. 18 (18), 3726–3738.

Lighthill, M.J., 1969. Dynamic response of the Indian ocean to the onset of the southwest monsoon. Phil. Trans. Roy. Soc. Lond. Math. Phys. Sci. 265, 45–92.

Lozovatsky, I., Wijesekera, H., Jarosz, E., Lilover, M.J., Pirro, A., Silver, Z., Centurioni, L., Fernando, H.J.S., 2016. A snapshot of internal waves and hydrodynamic instabilities in the southern Bay of Bengal. J. Geophys. Res.: Oceans 121 (8), 5898–5915.

Luther, M.E., O'Brien, J.J., 1985. A model of the seasonal circulation in the Arabian Sea forced by observed winds. Prog. Oceanogr. 14, 353–385.

McPhaden, M.J., 1982. Variability in the central Indian ocean. Part I: ocean dynamics. J. Mar. Res. 40, 157–176.

McPhaden, M.J., Proehl, J.A., Rothstein, L.M., 1986. The interaction of equatorial Kelvin waves with realistically sheared zonal currents. J. Phys. Oceanogr. 16 (9), 1499–1515.

Miyama, T., McCreary Jr., J.P., Jensen, T.G., Sengupta, D., Senan, R., 2006. Dynamics of biweekly oscillations in the equatorial Indian ocean. J. Phys. Oceanogr. 36, 827–846. https://doi.org/10.1175/JPO2897.1.

Mooers, C.N.K., 1973. A technique for the cross spectrum analysis of pairs of complex-valued time series, with emphasis on properties of polarized components and rotational invariants. Deep-Sea Res. 20 (12), 1129–1141.

Moore, D.W., 1968. Planetary-gravity Waves in an Equatorial Ocean. Ph.D. thesis. Harvard Univ., Cambridge, Mass.

Moore, D.W., McCreary Jr., J.P., 1990. Excitation of intermediate frequency equatorial waves at a western ocean boundary: with application to observations from the Indian Ocean. J. Geophys. Res. 95 (C4), 5219–5231. https://doi.org/10.1029/JC095iC04p05219.

Nagura, Motoki, McPhaden, Michael J., 2010. Wyrtki jet dynamics: seasonal variability. J. Geophys. Res.: Oceans 115, C7.

Oliver, E.C.J., Thompson, K.R., 2010. Madden-Julian Oscillation and sea level: local and remote forcing. J. Geophys. Res. 115 https://doi.org/10.1029/2009JC005337. C01003.

Oort, A.H., Ascher, S.C., Levitus, S., Peixoto, J.P., 1989. New estimates of the available potential energy in the world ocean. J. Geophys. Res. 94 (C3), 3187–3200.

Pedlosky, J., 1987. Geophysical Fluid Dynamics, second ed. SpringerVerlag.

Pirro, A., Fernando, H.J.S., Wijesekera, H.W., Jensen, T.G., Centurioni, L.R., Jinadasa, S.U.P., 2020. Eddies and Currents in the Bay of Bengal during summer monsoons. Deep Sea Research Part II: Topical Studies in Oceanography 104728.

Qiu, B., Mao, M., Kashino, Y., 1999. Intraseasonal variability in the Indo-Pacific throughflow and the regions surrounding the Indonesian Seas. J. Phys. Oceanogr. 29, 1599–1618.

Rajendran, K., Kitoh, A., 2006. Modulation of tropical intraseasonal oscillations by ocean–atmosphere coupling. J. Clim. 19 (3), 366–391.

Rath, S., Vinayachandran, P.N., Behara, A., Neema, C.P., 2017. Dynamics of Summer Monsoon Currents Around Sri Lanka arXiv preprint arXiv:1711.03311.

Raymond, D.J., Esbensen, S.K., Paulson, C., Gregg, M., Bretherton, C.S., Petersen, W.A., Cifelli, R., Shay, L.K., Ohlmann, C., Zuidema, P., 2004. EPIC2001 and the coupled ocean–atmosphere system of the tropical east Pacific. Bull. Am. 85 (9), 1341–1351.

Reppin, J., Schott, F.A., Fischer, J., Quadfasel, D., 1999. Equatorial currents and transports in the upper central Indian ocean: annual cycle and interannual variability. J. Geophys. Res. Oceans 104 (C7), 15495–15514.

Rossby, T., 1987. On the energetics of the gulf stream at 73°W. J. Mar. Res. 45, 59–82.

Roxy, M., Tanimoto, Y., 2007. Role of SST over the Indian Ocean in influencing the intraseasonal variability of the Indian summer monsoon. J. Meteorol. Soc. Jpn. 85 (3), 349–358.

Sengupta, D., Retish, S., Goswami, B.N., 2001. Origin of intraseasonal variability of circulation in the tropical central Indian Ocean. Geophys. Res. Lett. 28 (7), 1267–1270.

Sengupta, D., Senan, R., Murty, V.S.N., Fernando, V., 2004. A biweekly mode in the equatorial Indian Ocean. J. Geophys. Res. 109 https://doi.org/10.1029/2004JC002329. C10003.

Subrahmanyam, B., Robinson, I.S., Blundell, J.R., Challenor, P.G., 2001. Indian Ocean Rossby waves observed in TOPEX/POSEIDON altimeter data and in model simulations. Int. J. Rem. Sens. 22 (1), 141–167, 2001.

Szabo, D., Weatherly, G.L., 1978. Energetics of kuroshio south of Japan. J. Mar. Res. 37, 531–556.

Thomson, R.E., Emery, W.J., 2014. Data Analysis Methods in Physical Oceanography. Newnes.

Thum, N., Esbensen, S.K., Chelton, D.B., McPhaden, M.J., 2002. Air–sea heat exchange along the northern sea surface temperature front in the eastern tropical Pacific. J. Clim. 15 (23), 3361–3378.

Vecchi, G.A., Harrison, D.E., 2002. Monsoon breaks and subseasonal sea surface temperature variability in the Bay of Bengal. J. Clim. 15 (12), 1485–1493.

Vecchi, G.A., Harrison, D.E., 2004. Interannual Indian rainfall variability and Indian Ocean sea surface temperature anomalies. In: Earth Climate: the Ocean-Atmosphere Interaction, Geophys. Monogr., vol. 147 American Geophysical Union, pp. 247–260.

Vialard, J., Shenoi, S.S.C., McCreary, J.P., Shankar, D., Durand, F., Fernando, V., Shetye, S.R., 2009. Intraseasonal response of the northern Indian Ocean coastal waveguide to the Madden-Julian Oscillation. Geophys. Res. Lett. 36 https://doi.org/10.1029/2009GL038450. L14606.

Vinayachandran, P.N., Yamagata, T., 1998. Monsoon response of the sea around Sri Lanka: generation of thermal domes and anticyclonic vorticies. J. Phys. Oceanogr. 28, 1946–1960.

Vinayachandran, P.N., Masumoto, Y., Mikawa, T., Yamagata, T., 1999. Intrusion of the southwest monsoon current into the Bay of Bengal. J. Geophys. Res. Oceans 104 (C5), 11077–11085.

Waliser, D.E., Murtugudde, R., Lucas, L.E., 2003. Indo-pacific ocean response to atmospheric intraseasonal variability: 1. Austral summer and the madden-julian oscillation. J. Geophys. Res.: Oceans 108 (C5).

Waliser, D.E., Murtugudde, R., Lucas, L.E., 2004. Indo-Pacific Ocean response to atmospheric intraseasonal variability: 2. Boreal summer and the Intraseasonal Oscillation. J. Geophys. Res.: Oceans 109 (C3).

Webber, B.G.M., Matthews, A.J., Heywood, K.J., 2010. A dynamical ocean feedback mechanism for the Madden-Julian Oscillation. Q. J. R. Meteorol. Soc. 136, 740–754. https://doi.org/10.1002/qj.604.

Webber, B.G.M., Stevens, D.P., Matthews, A.J., Heywood, K.J., 2012. Dynamical ocean forcing of the Madden–Julian Oscillation at lead times of up to five months. J. Clim. 25, 2824–2842. https://doi.org/10.1175/JCLI-D-11-00268.1.

Webster, P.J., Magaña, V., Palmer, T., Shukla, J., Tomas, R., Yanai, M.U., Yasunari, T., 1998. Monsoons: processes, predictability, and the prospects for prediction. J. Geophys. Res. 103 (C7), 14,451– 14,510.

Weisberg, R.H., Weingartner, T.J., 1988. Instability waves in the equatorial Atlantic Ocean. J. Phys. Oceanogr. 18 (11), 1641–1657.

Wijesekera, H.W., Shroyer, E., Tandon, A., Ravichandran, M., Sengupta, D., Jinadasa, S.U.P., Fernando, H.J.S., Agarwal, N., Arulananthan, K., Bhat, G.S., others, 2016a. ASIRI: an Ocean- atmosphere initiative for Bay of Bengal. Bull. Am. Meteorol. Soc. 1859–1884. https://doi.org/10.1175/BAMS-D-14-00197.1.

Wijesekera, H.W., Teague, W.J., Wang, D.W., Jarosz, E., Jensen, T.G., Jinadasa, S.U.P., Fernando, H.J.S., Hallock, Z.R., 2016b. Low-frequency currents from deep moorings in the southern Bay of Bengal. J. Phys. Oceanogr. 46 (10), 3209–3238.

Wijesekera, H.W., Teague, W.J., Jarosz, E., Wang, D.W., Jensen, T.G., Jinadasa, S.U.P., Fernando, H.J.S., Centurioni, L.R., Hallock, Z.R., Shroyer, E.L., Moum, J.N., 2016c. Observations of currents over the deep southern Bay of Bengal—with a little luck. Oceanography 29 (2), 112–123. https://doi.org/10.5670/oceanog.2016.44.

Wijesekera, H.W., Teague, W.J., Jarosz, E., Wang, D.W., Fernando, H.J.S., Hallock, Z.R., 2019. Internal tidal currents and solitons in the southern Bay of Bengal. Deep Sea Res. Part II Top. Stud. Oceanogr. (in press); this DSR-II volume).

Wyrtki, Klaus, 1973. An equatorial jet in the Indian Ocean. Science 181 (4096), 262–264.

Yu, L., O'Brien, J.J., Yang, J., 1991. On the remote forcing of the circulation in the Bay of Bengal. J. Geophys. Res.: Oceans 96 (C11), 20449–20454.